Space Weather

RESEARCH ARTICLE
10.1029/2025SW004659

Evidence and Causes of an Unusual Super Plasma Bubble Occurrence During Weak Geomagnetic Conditions Over Europe

Chandan Kapil[1], Mani Sivakandan[1], Jorge Chau[1], Gopi K. Seemala[2], and David Altadill[3]

[1]Leibniz Institute of Atmospheric Physics, University of Rostock, Rostock, Germany, [2]Indian Institute of Geomagnetism, Navi Mumbai, India, [3]Observatori de L'Ebre (OE), CSIC–Universitat Ramon Llull, Roquetes, Spain

Key Points:

- An unusual super plasma bubble (SPB) was observed during a minor geomagnetic storm over the African-European region
- Highlight on the cause of the rate of change of the total electron content index using multiple instruments like SWARM, GOLD, ionosonde, magnetometer, etc
- SPB is primarily driven by the combined effect of post-sunset pre-reversal enhancement and prompt penetration electric field (PPEF) induced E × B

Supporting Information:

Supporting Information may be found in the online version of this article.

Correspondence to:

M. Sivakandan,
skandanm89@gmail.com;
mani@iap-kborn.de

Citation:

Kapil, C., Sivakandan, M., Chau, J., Seemala, G. K., & Altadill, D. (2026). Evidence and causes of an unusual super plasma bubble occurrence during weak geomagnetic conditions over Europe. *Space Weather*, *24*, e2025SW004659. https://doi.org/10.1029/2025SW004659

Received 2 AUG 2025
Accepted 7 JAN 2026

Author Contributions:

Conceptualization: Mani Sivakandan
Data curation: Chandan Kapil
Formal analysis: Chandan Kapil, Mani Sivakandan
Funding acquisition: Chandan Kapil, Jorge Chau
Investigation: Chandan Kapil, Mani Sivakandan
Methodology: Chandan Kapil, Mani Sivakandan
Project administration: Jorge Chau
Supervision: Mani Sivakandan, Jorge Chau, Gopi K. Seemala

Abstract Using data from a cluster of ground-based global navigation satellite system, we observed spatially extended enhanced ROTI over the European longitudes during a weak geomagnetic storm (Dst ≈ −50 nT) on 4 November 2023. The enhanced ROTI is extended over an extensive geographical latitudinal range of 46°N. Further analysis using other simultaneous ground-based and satellite measurements reveals that the ROTI enhancement is caused by the super plasma bubble (SPB). For instance, a strong range spread and depletion in total electron content (TEC) were observed in the enhanced ROTI regions. Following this, depletion in TEC and OI135.6 nm irradiance was also observed along similar longitudes and latitudes on the African continent. Simultaneous Swarm-A and C electron density showed plasma depletion between 15°S and 31°N at 10°E, which agrees with the enhanced ROTI data as well. To explore the cause of this enhanced ROTI, the prompt penetration equatorial electric field model (PPEEFM) PPEEFM and magnetometer data have been analyzed. We found a sharp decrease in the geomagnetic field during the evening hours, which suggests the ingression of the prompt penetration electric field (PPEF). The PPEF arrival time coincides with the post-sunset pre-reversal enhancement; consequently, an SPB was generated. This study provides observational evidence of SPB in weak geomagnetic conditions, shedding light on the causative mechanism.

Plain Language Summary Depletion in the plasma density is commonly observed in the equatorial ionosphere during nighttime, called equatorial plasma bubbles (EPB). In general, EPB is a severe threat to satellite-based communication and navigation systems. Thus, it makes EPB a special phenomena that need to be understood for better space weather forecasting. Most often, EPB extends from the geomagnetic equator to the equatorial ionization anomaly crest (±15°–20°) during the geomagnetic quiet conditions. Occasionally, they can extend to mid-latitudes during severe geomagnetic activity, classified as a super plasma bubble (SPB). We observed an SPB over Europe during a weak geomagnetic storm on 04 November 2023. With the ground- and satellite-based multi-observations, we found the latitude and longitude extension of the SPB is 46°N and 10°W–10°E, respectively. Moreover, with the help of the empirical electric field model and magnetometer observations, we report the cause of the observed SPB. This study provides observational evidence for the occurrence of the SPB even in weak gemagnetic conditions.

1. Introduction

Plasma density has a more pronounced perturbation at the low (0°N–30°N) and higher latitudes (60°N–90°N), mainly due to the nearly parallel and perpendicular orientation of the Earth's magnetic field that supports the growth of plasma instabilities. Equatorial plasma bubbles (EPB) are one of the prominent plasma density perturbations in the equatorial and low-latitude ionosphere, which is a manifestation of reductions in plasma density across varying scale sizes from a few centimeters to a few hundred kilometers. The EPB is generated at the bottom of the F-region and evolves vertically 1,000 km, even beyond. Generally, EPB are confined within a narrow band of dip latitudes, typically within ±20° during the quiet, low solar activity conditions (Burke et al., 2004; Seemala & Valladares, 2011). These EPB are manifested as ionograms showing as dispersed echoes, plumes on VHF radar maps, intensity bite-outs in the nighttime 630 nm airglow intensity, and density depletions in the in situ satellite measurements and scintillations in VHF/L band satellite beacon signals. The EPB is primarily governed by the Rayleigh-Taylor (R-T) instability initiated at the bottom side of the F-region (Dungey, 1956). According to the linear R-T instability mechanism, the growth rate is directly proportional to the vertical gradient of the electron density and inversely proportional to the ion-neutral collision frequency. Later, it was understood that in addition

Visualization: Chandan Kapil, Mani Sivakandan
Writing – original draft: Chandan Kapil
Writing – review & editing: Chandan Kapil, Mani Sivakandan, Jorge Chau, Gopi K. Seemala, David Altadill

to the above factors, the R-T instability growth rate is also controlled by various other factors such as trans-equatorial neutral winds, zonal electric fields, vertical and horizontal ionospheric density gradients, E-F region electric field coupling, and chemical recombination (Sultan, 1996). For instance, enhancement in the eastward electric field followed by the sunset, referred to as the pre-reversal enhancement (PRE), drives upward motions of the bottom of the F layer to higher heights at the equator, which causes the large vertical gradient in the plasma density that has high correlation with the EPB onset (Ghosh et al., 2020). Investigations showed that wave undulations at the bottom of the ionosphere also play a key role in the initial seeding of the EPB (Narayanan et al., 2012; Patra et al., 2013; Singh et al., 1997; Sivakandan et al., 2019; Tsunoda, 2010). In addition, studies suggested that the possibility of EPB occurrence is higher during the intense equatorial electrojet (EEJ) event; however, during the counter electrojet (CEJ) condition, the generation is suppressed (Akiyama et al., 2019; Ghosh et al., 2020).

Spread F is extensively documented and researched in the equatorial and low-latitude regions, primarily through the R-T instability lens. Additionally, it has garnered attention in midlatitude areas, particularly where its onset is often linked to the Perkins instability mechanism (Shiokawa et al., 2003; Sivakandan et al., 2020). The mid-latitude spread-F (MLSFs) has been associated with geomagnetic storms, medium-scale traveling ionospheric disturbances (MSTIDs), and consequent elevations in the F region (Paul et al., 2018, 2022). However, some studies reported instances where MLSFs are observed without the presence of MSTIDs (Kelley et al., 2010; Shiokawa et al., 2003). This suggests that MLSFs are not only caused by the MSTIDs but can also be caused by other sources, such as geomagnetic disturbances and mid-latitude extension of the EPB known as a super plasma bubble (SPB). As reported in the earlier studies, SPBs differ from plasma bubbles in terms of their latitudinal extent, which extends beyond the equatorial ionization anomaly. They are characterized by moderate to severe electron density depletions and can potentially induce scintillations in the radio signals of the global navigation satellite system (GNSS) (Cherniak & Zakharenkova, 2016; Ma & Maruyama, 2006).

Using the rate of TEC index (ROTI) observational evidence, the SPB was first reported by (Ma & Maruyama, 2006) over the Asian sector. Since then, several studies have reported the SPB during moderate and strong geomagnetic storm events at different solar activity conditions (Aa et al., 2018; Calabia et al., 2024; Cherniak & Zakharenkova, 2016, 2022; Martinis et al., 2015; Sori et al., 2022). For example, Cherniak and Zakharenkova (2016) reported the occurrence of SPB during a severe geomagnetic storm event over Europe in a high solar activity year of 2015. Similarly, Sori et al. (2022) studied the conjugacy of SPB in the Asian sector during a geomagnetic storm on 01 March 2013. These studies postulate that the geomagnetic storm-associated prompt penetration electric field (PPEF) could be the main driver of the observed SPBs. However, recently, Rajesh et al. (2022) reported an SPB event during the eruption of the Hunga Tonga volcano and argued that the combination of reduced E-region conductivity by volcano-induced waves and enhanced F-region wind and reduced ion drag over the equatorial ionization anomaly (EIA) intensified the PRE. This strong PRE leads to the volcanically induced SPB. So far, SPB has been reported only during moderate (Dst ≈ -50 nT to (Dst ≈ -100 nT) and severe geomagnetic storms (Dst > -100 nT), strong seismic events such as the Hunga Tonga eruption (Aa et al., 2022; Campuzano et al., 2023; Cherniak & Zakharenkova, 2016; Katamzi-Joseph et al., 2017; Li et al., 2018).

In the present study, using ground-based GNSS-total electron content (TEC), ROTI, ionograms, and satellite measurements, we document observational evidence of SPB over the western African-European region, and its probable underlying causes during a weak geomagnetic storm (Dst ≈ -50 nT) on 4 November 2023. During this event, the Kp value was below 4, and the ROTI values exceeded 0.5 TECU/min in the mid-latitudes, which is an indication of plasma irregularities. Subsequently, a severe storm occurred on 5 November 2023, with a Kp value of 8; however, no SPB was observed. Thus, this study focuses on exploring the presence and absence of SPB on 4 and 5 November 2023, respectively, as well as plausible physical reasoning. The data set and methodology are briefed in Section 2. The results and discussions are given in Sections 3 and 4, respectively. The overall summary and conclusions are provided in Section 5.

2. Data and Methodology

In this study, we used data from multiple instruments, located across the African-European region, and an empirical model. Figure 1 shows the locations of all the stations used in the present study, including ionosondes,

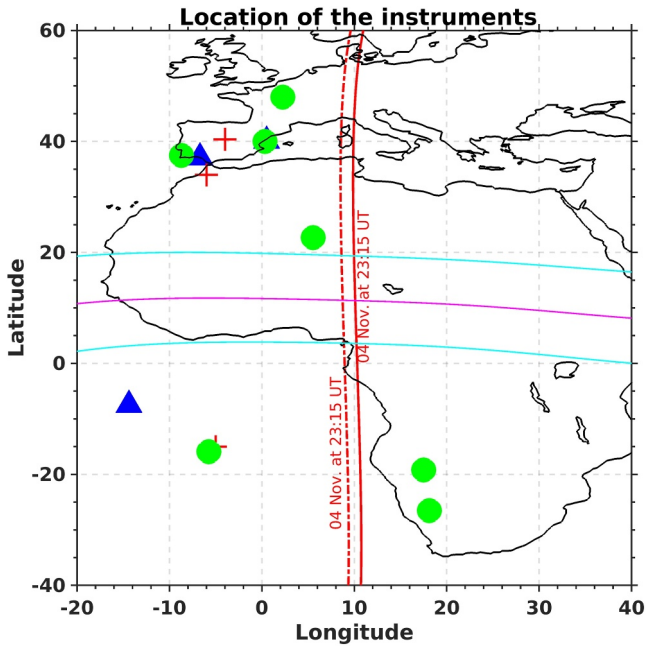

Figure 1. Locations of the ground-based instruments and Swarm satellite passes across the African-European sector on 04 November 2023. The symbols like triangle (blue), plus (red), and circle (green) denote the ionosondes, IGS-GNSS receivers, and Magnetometers location, respectively. The thick red (dotted) line indicates the Swarm-A (Swarm-C) passage across the African-European region. The magenta line indicates the geomagnetic dip equator, and the cyan lines represent the ±10° geomagnetic dip latitudes estimated using IGRF.

magnetometers, and International GNSS services (IGS) stations. Brief information about each instrument is given below.

2.1. Global Navigation Satellite System

Ionospheric irregularities in the mid-latitudes are assessed through their impact on the phase/amplitude of received GNSS-based signals. The two GNSS-based metrics are the Rate of TEC (ROT) change and the ROT index (ROTI). ROT reflects the rate of change of TEC over time, serving as an indicator of amplitude fluctuation activity. ROT is expressed in TEC units per minute, with 1 TECU equivalent to 10^{16} electrons per square meter. ROTI represents the standard deviation of ROT within a five-minute interval (Pi et al., 1997). The slant TEC is the integral of electron density along the line from a ground-based receiver to a GNSS satellite. In this study, we have used vertical TEC as provided by the Nagoya University and IGS services. ROTI gauges the severity of GNSS amplitude fluctuations and identifies the presence of ionospheric irregularities. In addition, the perturbation component of the TEC (detrended TEC) is obtained by subtracting the 1-hr running average (average over ±30 min centered on the corresponding data) from the original TEC time series for each pair of satellites and receivers, which is used to identify the TIDs. These computed values correspond to the ionospheric piercing points along the receiver-satellite line-of-sight, assuming a thin ionospheric layer at 250 km altitude (Otsuka et al., 2002). In the present study, we used GNSS data sets in the African and European sectors operated by many data providers (https://stdb2.isee.nagoya-u.ac.jp/GPS/GPS-TEC/gnss_provider_list.html).

2.2. Swarm Satellite

We used in situ electron density (Ne) measurements from Swarm satellites to capture the topside ionospheric variabilities. The three Swarm satellites, A, B, and C, fly in different orbital configurations (two flying side by side at lower altitudes and the third at a slightly higher altitude). In this study, we used Swarm A and C measured in situ Ne and ROTI values. Swarm A and C satellites are twin satellites, flying at a mean altitude of 487.86 km and separated longitudinally at 1.4°, while Swarm B measures at a mean altitude of 519.98 km, as of 04 November 2023.

2.3. Ionosonde

To investigate the spread-F phenomenon, which involves frequency and range changes due to total reflection from large, tilted ionization surfaces (King, 1970) in mid-latitude regions, we utilized observations from two ionosondes located in Spain: Roquetes (40°N, 0.5°E; dip latitude: 36.93°) and El Arenosillo (37°N, 7°W; dip latitude: 31.62°). Additionally, we included measurements from an ionosonde on Ascension Island (7.95°S, 14.4°W; dip latitude: −23.41°), which is situated in the southern hemisphere's low-latitude region.

2.4. Prompt Penetration Electric Field Model

We also used an empirical model named the prompt penetration equatorial electric field model (PPEEFM) developed by the University of Colorado (Manoj & Maus, 2012). The PPEEFM uses a transfer function derived from 8 years of ionospheric electric field data from the ACE satellite and the JULIA radar, as well as magnetometer data from the CHAMP satellite. This model also provides the climatology of the electric field, which is based on 6 years of magnetometer measurements from the CHAMP satellite. The model accepts as input a time and location, produces the best estimate of the electric field for these parameters, and provides a quiet and penetrated electric field at a latitudinal span of ±20°. We used the PPEEFM model to analyze the polarity of PPEF during temporal observation of ROTI and spread F, as the penetrated electric field during PPEF events is instantaneously injected at equatorial-low latitudes through the atmospheric waveguide (Astafyeva et al., 2016).

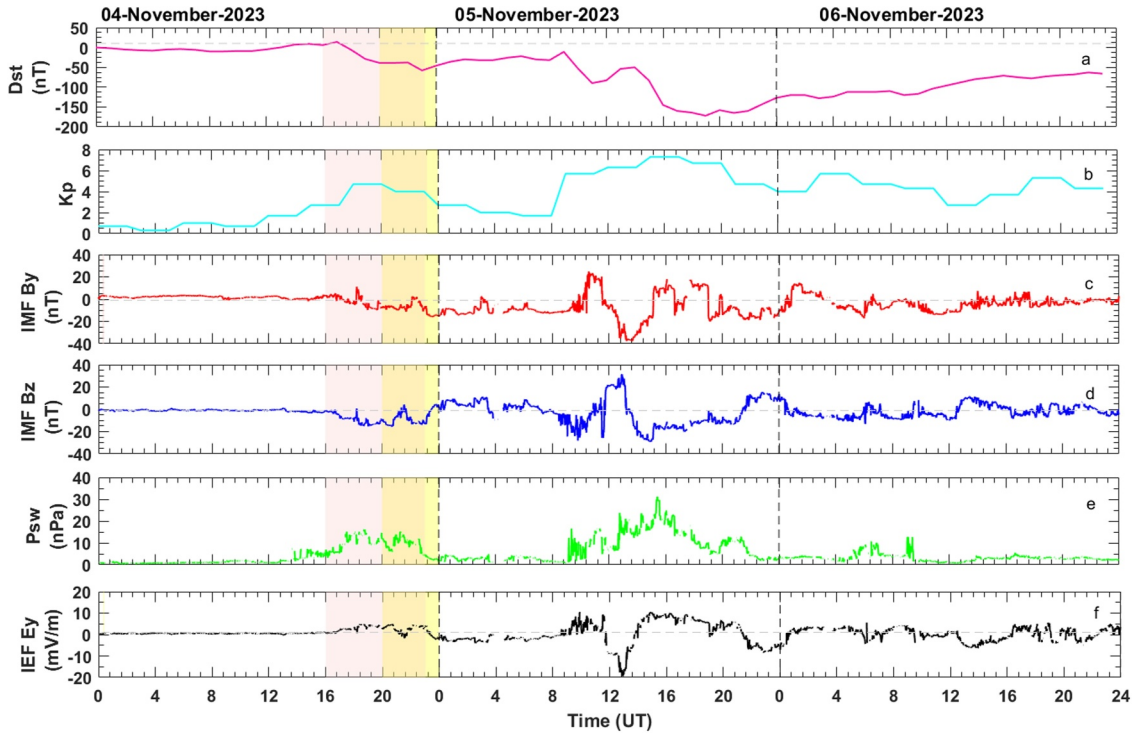

Figure 2. The variation of Dst (a), Kp (b), interplanetary magnetic field (IMF) By (c), IMF Bz (d), solar pressure (e), and interplanetary electric field electric field (f) are shown for 4–6 November 2023. The black dashed line shows the separation between the days. The yellow-shaded region indicates the duration of the enhanced ROTI values observed over Europe, whereas the red-shaded region indicates the main phase of the weak geomagnetic storm of 4 November 2023.

2.5. GOLD Observations

NASA's Global-scale Observations of the Limb and Disk (GOLD) mission observes Earth's far-ultraviolet (FUV) airglow emissions from geostationary orbit. The GOLD spectrograph provides a unique opportunity to study EPB through full-disk observations. GOLD is equipped with two identical imaging spectrographs that capture Earth's FUV emissions in the wavelength range of approximately 132–162 nm. It measures the column-integrated emission rate along the line of sight, enabling unambiguous observation of the spatial and temporal evolution of various ionospheric and thermospheric features visible to the instrument. The Level 1C (L1C) product constitutes the primary science data generated by GOLD. Nighttime L1C disk images are acquired every 15 min and are binned to a spatial resolution of approximately 96 km by 80 km at nadir. In this study, only the nighttime disk images of atomic oxygen at 135.6 nm (NI1 data) are used. When geolocating the pixels, the nighttime peak emission altitude for OI 135.6 nm is assumed to be 300 km (Cai et al., 2020; Eastes et al., 2017).

2.6. Magnetometer

We analyzed magnetometer data to examine variations in the H, *X*, and Y components of the geomagnetic field. The H-component values used in this study, obtained from INTERMAGNET, do not include a baseline. To enable comparison and normalization, the H values were scaled using the formula

$$H/3438 \times 10000,$$

where 3438 nT represents the reference annual mean value. This scaling highlights relative variations in the geomagnetic field.

In this study, one-minute resolution magnetometer data from the European-African region are marked by the green circles in Figure 1 and are analyzed to show simultaneous signatures of the PPEF from mid-to low-latitude regions, as illustrated in Figure 2. The stations used are: clf (48°N, 2.26°E), ebr (40°N, 0.33°E), stt (37.5°N, 8.72°W), tam (22.7°N, 5.53°E), she (15.9°S, 5.74°W), tsu (19.20°S, 17.58°E), and kmh (26.54°S, 18.11°E), all of

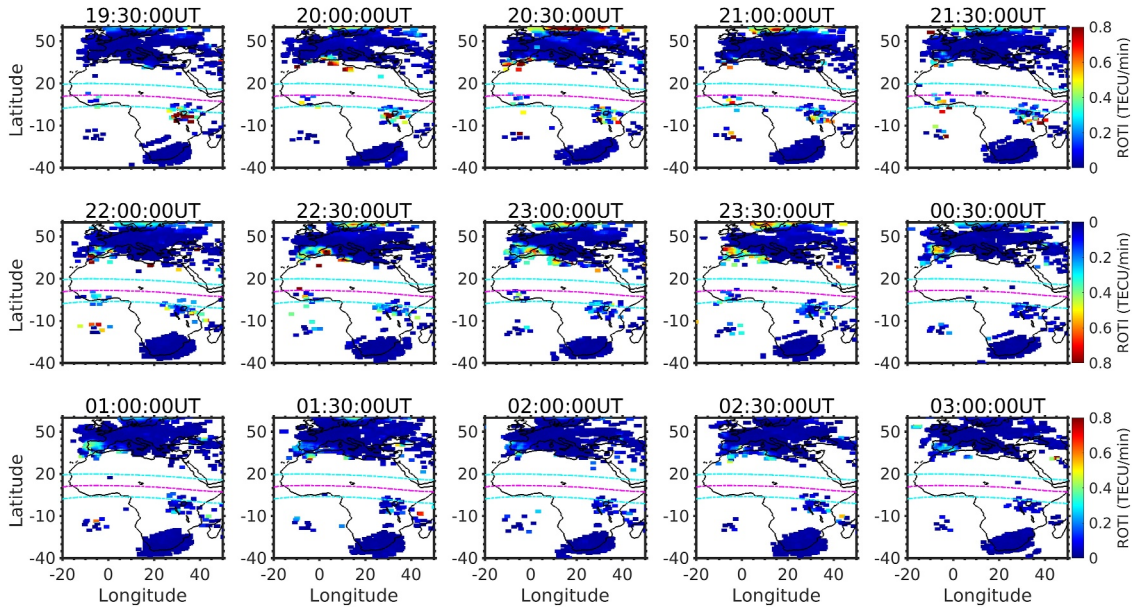

Figure 3. The Variation of ROTI over the African and European region on 04–05 November 2023. In these Figures magenta dotted line denotes the geomagnetic equator, and the Cyan lines represent the ±10° geomagnetic latitudes.

which are part of the International Real-time Magnetic Observatory Network (INTERMAGNET) (Kim & Chang, 2018). Prompt penetration electric field signatures are rapidly mapped from high to low latitudes (Bagiya et al., 2017). Therefore, these stations were selected to analyze the PPEF signatures across the European-African region.

3. Results

3.1. Observational Evidence of Super Plasma Bubble in a Weak Geomagnetic Event

In this study, we investigate a super plasma bubble (SPB) event observed on 4 November 2023. On this day, a geomagnetic storm impacted the Earth's magnetosphere, beginning with a southward turning of the interplanetary magnetic field (IMF) B_z around 16:00 UT on 4 November 2023. The disturbance storm time (Dst) index reached a minimum of −50 nT, and the K_p index reached a value of 4 around 20:00 UT, as shown in Figures 2a and 2b. The main phase starts around 16:00 UT with a marginal increase of Dst around 16:40 UT and then followed by negative Dst values, of the storm persisted until 23:30 UT, and this event is classified as a weak geomagnetic storm (Collado-Villaverde et al., 2024). According to the National Oceanic and Atmospheric Administration classification, it corresponds to a G1-level geomagnetic storm—the weakest storm category based on the K_p index.

This event was followed by a severe geomagnetic storm on 5 November 2023, around noon, when Dst reached −160 nT by 17:00 UT, as shown in Figure 2a. The recovery phase continued until 6 November 2023. Variations in solar wind and interplanetary parameters, including IMF components B_y and B_z, solar wind dynamic pressure, and the interplanetary electric field (IEF) E_y, are shown in Figures 2c–2f, respectively. The black dashed lines mark the day boundaries. The IMF B_z turned southward around 16:00 UT on 4 November and remained southward until about 21:00 UT. It then turned northward briefly between 21:00 and 22:00 UT before turning southward again for a short interval. Around midnight, B_z became persistently northward and remained so until the following morning. During this period, the solar wind dynamic pressure varied between 8 and 20 nPa, and the IEF E_y decreased to −5 mV/m.

Using GNSS measurements, we observed enhanced ROTI values in the European mid-latitudes on 4 November 2023, indicating the severity of mesoscale (less than 100 km) ionospheric irregularities in the F region. A few sample ROTI maps for every 30-min interval, starting from 19:30 UT (4 November) to 03:00 UT (5 November),

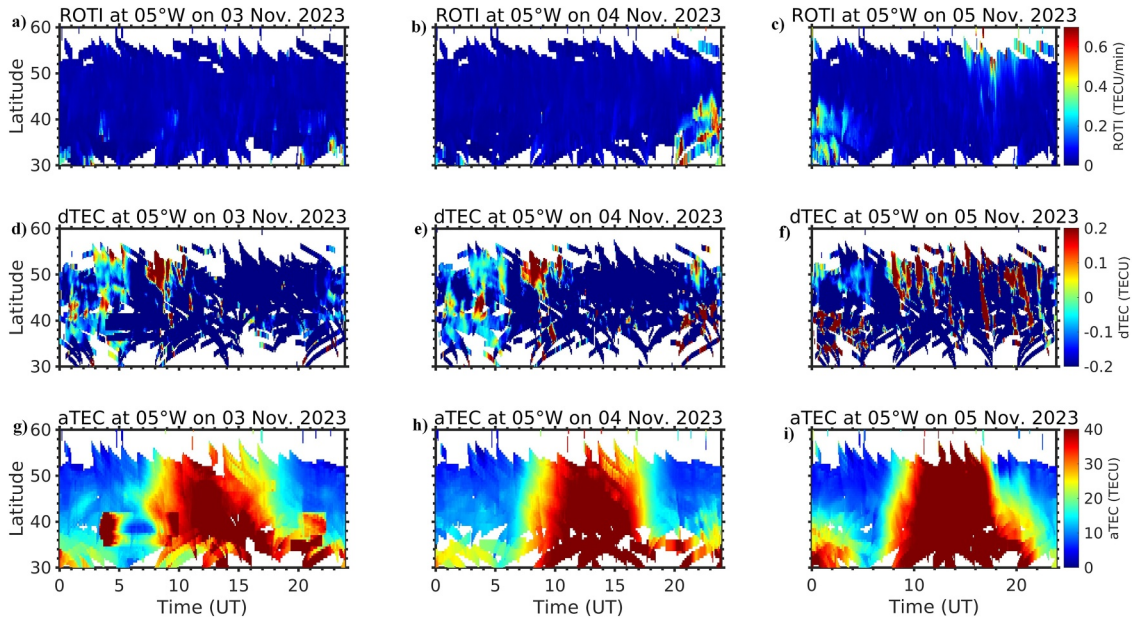

Figure 4. Keogram of ROTI (top panel), dTEC (middle panel), and absolute total electron content (absolute) centered at 5°E longitude on 03 (left), 04 (middle), and 05 (right) November 2023, respectively.

over the African and European sectors are shown in Figure 3. The temporal and spatial evolution of ROTI over Europe is presented as a movie in the Supporting Information S1.

The ROTI values surpassed 0.8 TECU/min and were confined between 10°W and 10°E longitudes, extending latitudinally up to 46°N around 5°W. Furthermore, the enhanced ROTI persisted for a long duration from 20:00 UT to 03:00 UT on 4–5 November 2023. In addition, we also observed ROTI enhancement above 55°N latitude, which was caused by auroral activity and is not the focus of this study. During this event, the Dst values continuously decreased until 23:30 UT (minimum of ≈ -50 nT) and then started to recover slowly. Moreover, as mentioned before, during the enhanced ROTI period on 4 November 2023, the K_p index did not exceed 4.

We examined the detrended TEC (dTEC) to identify possible nighttime MSTIDs, which are caused by plasma instabilities and are a potential source of enhanced ROTI values in the mid-latitude ionosphere. On this night, MSTID activity was not observed in the dTEC maps, indicating that the ROTI enhancement on 4 November was not caused by MSTIDs. Note that to confirm the presence of MSTIDs in dTEC data, the ionospheric community generally follows a few criteria: (a) the perturbation amplitude should exceed 0.2 TECU, and (b) at least three consecutive wave fronts should be visible in three consecutive maps (covering 15 min or more) (Tsugawa et al., 2018). Additionally, we examined the temporal evolution of the dTEC maps but could not identify any wavefronts. It is also worth noting that plasma irregularities can cause dTEC perturbations without exhibiting any periodic wave structures.

In order to illustrate the temporal and spatial (latitudinal and longitudinal) evolution of the enhanced ROTI values, we constructed north–south keograms centered at 5°W. A keogram represents a latitudinal (north–south) and/or longitudinal (east–west) cross-section of the ROTI values, arranged as a function of time. The north–south keograms of ROTI, dTEC, and aTEC centered at 5°W are shown in Figure 4 (top, middle, and bottom panels, respectively). Here in Figure 4, absolute TEC (aTEC) refers to the vertical TEC values as obtained from the sources discussed in Section 2.1.

Enhanced ROTI values in the mid-latitudes (>30°N) are observed in the keograms between 20:00 and 03:00 UT, with the maximum latitudinal extension appearing in the 5°W keogram, reaching up to 46°N geographic latitude on 4–5 November 2023 around midnight. The simultaneous dTEC keogram does not indicate any MSTID activity but shows enhanced dTEC values. Additionally, the aTEC exhibits a slight depletion; however, it is not significant because aTEC represents an integrated TEC value along the satellite path and thus corresponds to an average over multiple satellite passes at a given latitude and longitude. Consequently, immediate depletions are not

10.1029/2025SW004659

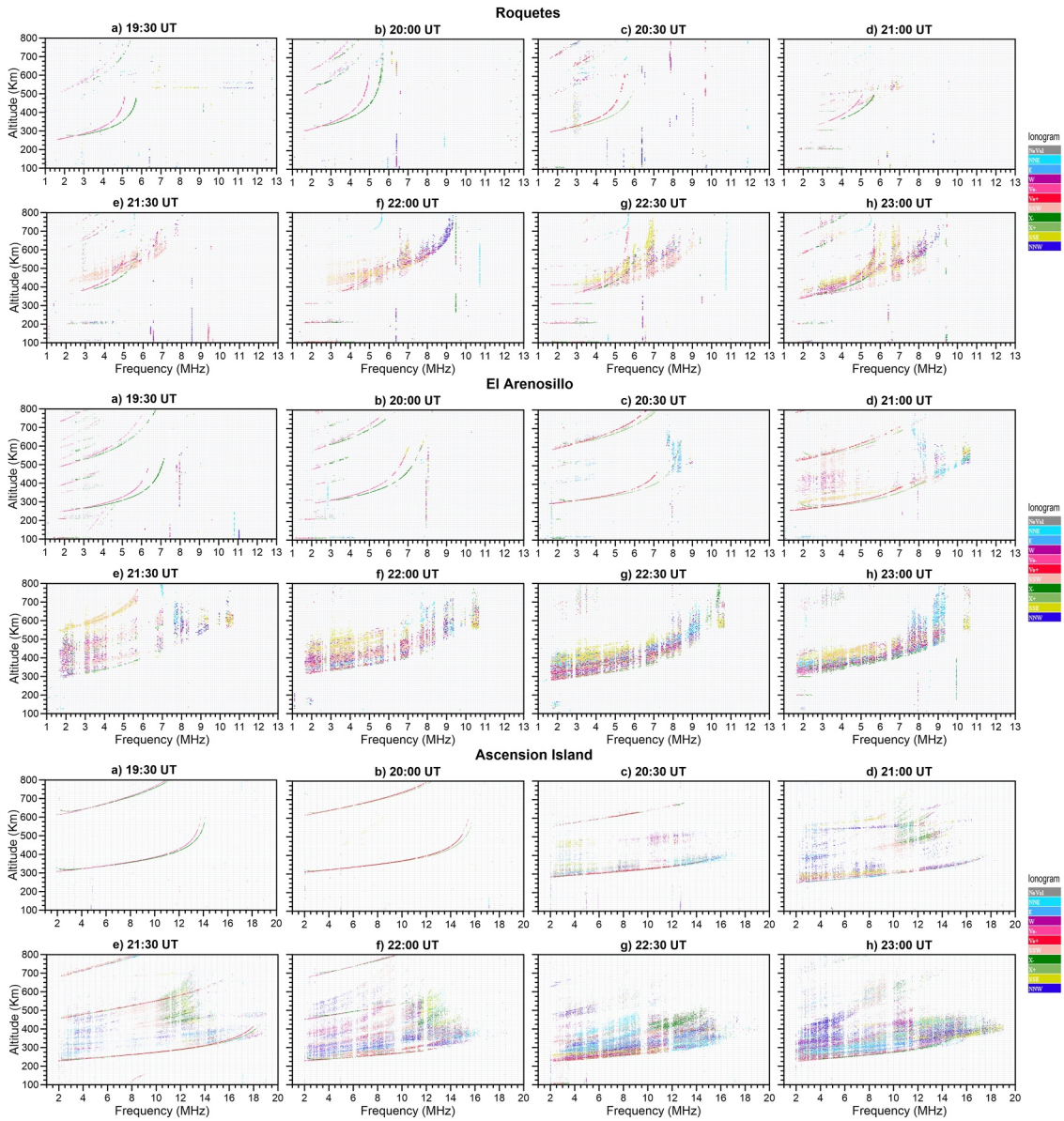

Figure 5. Ionograms for every 30 min obtained from three stations, namely Roquetes (top two rows), El Arenosillo (middle two rows) in southwestern Europe, and Ascension Island (bottom two rows) on 4 November 2023.

necessarily expected in the aTEC maps. Furthermore, the keograms did not show any enhancement on the night of 5 November 2023, despite the occurrence of a strong geomagnetic storm ($K_p > 8$).

In addition to the ROTI measurements, we also examined other simultaneous observations such as ionograms, GOLD OI 135.6 nm radiance, and vertical TEC derived from single-station GPS data to explore the latitudinal and longitudinal extent of the enhanced ROTI-associated processes, that is, plasma bubbles. The ionograms were obtained from the Digisonde networks, as shown in Figure 5. We identified strong range spread-F (RSF) signatures in three Digisonde ionograms located at Roquetes (40°N, 0.5°E), El Arenosillo (37°N, 7°W) in southwestern Europe, and Ascension Island (7.95°S, 14.4°W) on 4 November 2023, as shown in Figure 5. The top two rows, middle two rows, and bottom two rows of Figure 5 correspond to the ionograms starting at 19:30 UT every 30 min for Roquetes, El Arenosillo, and Ascension Island, respectively. All these stations display strong RSF signatures which start around 20:30, 21:00, and 21:30 UT in the Ascension Island, El Arenosillo, and Roquetes. The timing of the observation is in good agreement with the longitudinal difference of the ionosonde station

10.1029/2025SW004659

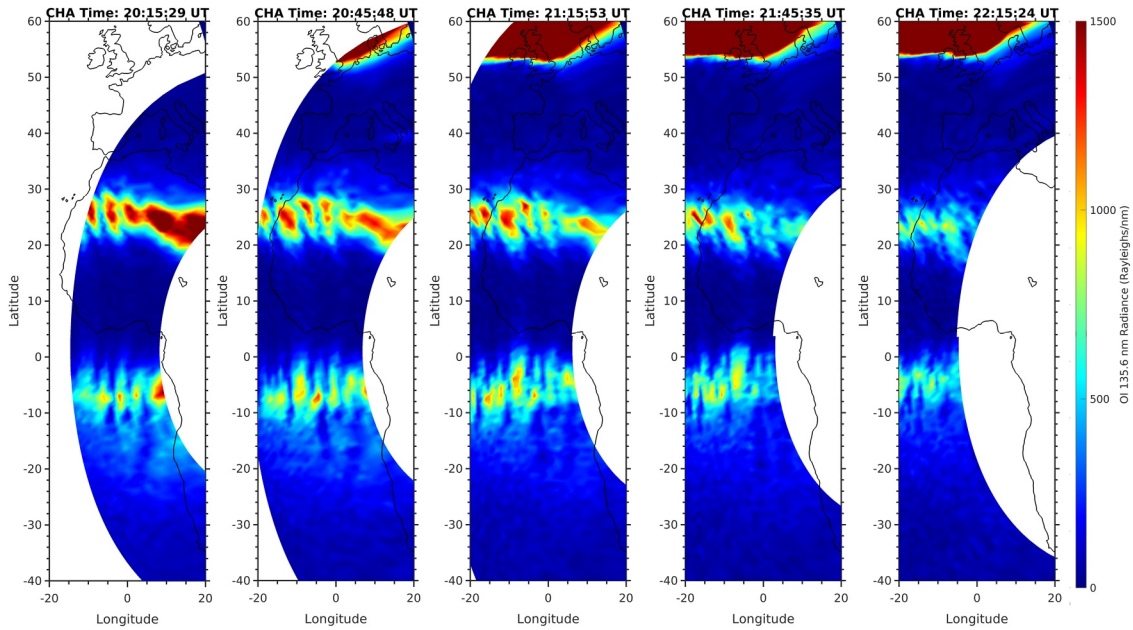

Figure 6. GOLD OI135.6 nm radiance observed by the Channel-A and B, note that channel A measures the northern hemisphere and B observes the southern hemisphere, over the African-European sector. They have a slight time difference of 3 min. In the figures, we used channel A time as a reference time.

locations. These RSF occurrence is persistent till 02:00 UT in the Ascension Island and 03:00 UT in the European stations. These observations are in good agreement with the duration of the ROTI enhancement observed over southwestern Europe. The Digisonde data used in this study are publicly available through the GIRO web portal: https://giro.uml.edu/ionoweb/. It is also worth noting that the local times of these ionosonde stations differ by approximately 30 min.

The RSF shown in the ionograms signifies the signatures of the plasma bubbles (Booker, 1938). It should be mentioned that spread F in mid-latitudes is also caused by traveling ionospheric disturbances (particularly frequency spread F, Paul et al., 2018, 2023). Occasionally, MSTIDs can also cause a weak RSF. However, from the dTEC maps, we could not witness any MSTIDs activity. On the other hand, we have observed intense plasma bubbles in the low latitude which extend beyond the EIA crest as observed in the GOLD OI135.6 nm radiance images, as shown in Figure 6. It should be mentioned here that due to the limitation of the spatial resolution, GOLD measurement did not capture the plasma depletion with a scale size below 100 km, which could be a reason we did not observe any depletion over the ROTI enhancement region.

Additionally, we also used a single station GNSS TEC measurement to investigate the depletions over the low and mid latitudes, as shown in Figure 7. The VTEC values are used from the International GNSS service (https://igs.org/wg/ionosphere/) TEC depletions are characterized by an abrupt reduction in TEC values over a certain period, followed by a gradual recovery, relative to previous TEC values (DasGupta et al., 1983; Kapil & Seemala, 2024). To avoid multi-path effects, we applied a cutoff of elevation angle in the GNSS satellite data to be above 15°. Figure 7 shows the GNSS stations located in Spain, Morocco, and Cabo Verde during the main phase of the geomagnetic storm on 04 November 2023. These observations provide additional evidence of plasma bubble activity in the western European-African sector. In addition, small-scale depletions are embedded within broader depletion regions as shown in Figure 7. The TEC values observed on 4 November 2023 are shown as a red solid line. For comparison with quiet-time conditions, TEC values are observed on 18 November 2023, which is a geomagnetically quiet day and, are plotted as a blue solid line. However, several small-scale depletions are visible within this depletion event. The red solid lines in Figure 7 for Spain, and Morocco, indicate distinct TEC depletions beginning around 22:30 UT, and 21:00 UT, respectively, continuing thereafter. The end of the depletion is represented by the magenta dashed line. The magnitudes of these depletions are relatively higher compared to the quiet-time values represented by the blue solid lines. The TEC depletions observed around 5°W longitude reflect the presence of plasma bubbles, which coincide temporally with the period of enhanced ROTI values shown in Figure 3.

10.1029/2025SW004659

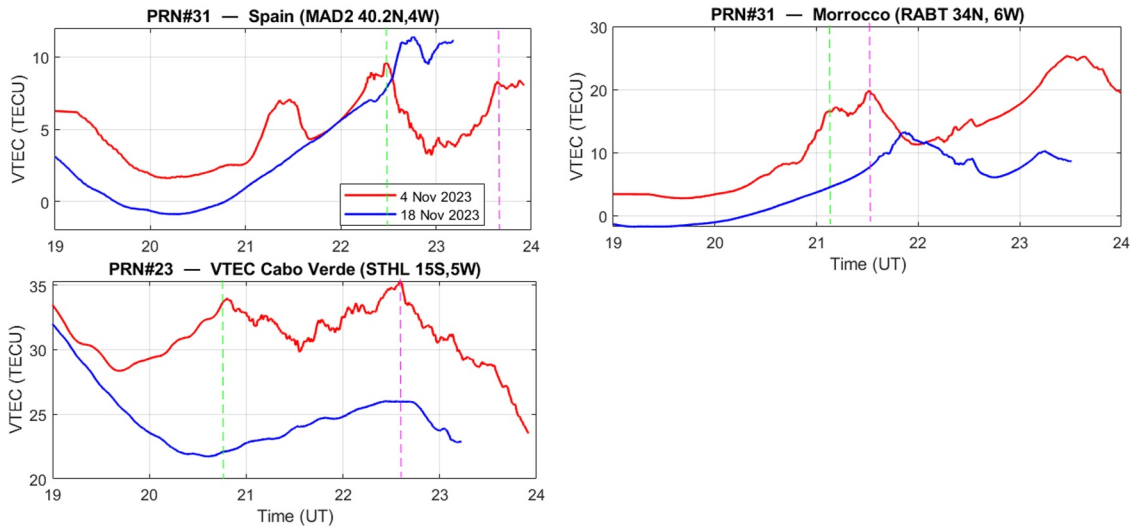

Figure 7. Single station global navigation satellite system vertical total electron content (VTEC) measured at three stations, namely MAD2 (Spain), STHL (Cabo Verde), and RABT (Morocco). The *x*-axis and the *y*-axis show time and VTEC, respectively. The red solid line shows the disturbed time, that is, 4 November 2023, whereas the blue line shows a chosen quiet time (18 Nov 2023) VTEC. The green and pink dashed line represents the start and end of the VTEC depletions.

To understand the plausible source of the enhanced ROTI over western Europe, we also analyzed in situ Swarm A and C satellites' measured electron densities from 02 to 05 November 2023, as shown in Figure 8. In these Figures, panel (a) shows the Swarm A (C) passes from 02 to 05 November 2023, shown in green, blue, red, and black solid (dotted) lines, and the equator crossing time of each pass is also indicated. Panels (b) and (c) show the in situ nighttime electron density (Ne) observed on these days. We observed the presence of plasma depletions on 02, 03, and 04 November, except on 05 November in the Swarm electron density measurement. Of which the deep depletion is observed on 02 November (Swarm-A, Figure 8b), and the largest latitudinal extension is observed on 04 November. On 04 November, the latitudinal extension of the plasma bubble reaches up to 31°N and 13°S, respectively. The observed depletion patterns and magnitude depend on the satellite's trajectory relative to the structure and orientation of the plasma bubbles. Therefore, the day-to-day variability in the strength (i.e., the steepness of the plasma bite-outs) of the plasma depletions observed by Swarm cannot be directly compared or interpreted without considering this geometrical dependence. For example, on 02 November, the depletion is very strong in Swarm-A; however, such a strong depletion is not seen in Swarm-C, though these two satellites are only separated by 1.5° longitude, shown in Figure 8a. As shown in Figures 8b and 8c, the extent of these depletions is significantly greater than that observed on other days, suggesting enhanced equatorial plasma instability during the event. Also, the magnitude and latitudinal extension of the EIA is symmetric and large on 04 November compared to all other days. Plasma depletions along the EIA were also observed on 03 November 2023; however, their latitudinal extent was smaller compared to those on 04 November 2023. Figures 8d and 8e show the corresponding ROTI values estimated from Swarm measurements, and Figure 8f represents the ROTI values derived from GNSS-TEC. It shows that the Swarm measurements are in good agreement with GNSS-ROTI values. This evidence suggests that the observed ROTI enhancement over Western Europe is due to low-latitude generated plasma bubbles. Furthermore, the GNSS-ROTI measurement shows that the maximum latitudinal extension of the observed plasma bubble reached up to 46°N geographic north around 5°W longitude (see Figures 4b and 4c). Such a large latitudinal extension is classified as an SPB (Cherniak & Zakharenkova, 2022; Ma & Maruyama, 2006).

4. Discussion

Typically, ROTI values remain below 0.4 TECU/min due to the shallow perturbations in the mid-latitude ionosphere (Kotulak et al., 2020). A recent study by Paul et al. (2024) investigated the relationship between ROTI and MLSFs and found that RSF occurred in all notable cases when ROTI values exceeded 0.2 TECU/min. Furthermore, these events coincided with the occurrence of nighttime MSTIDs. They proposed that gravity waves

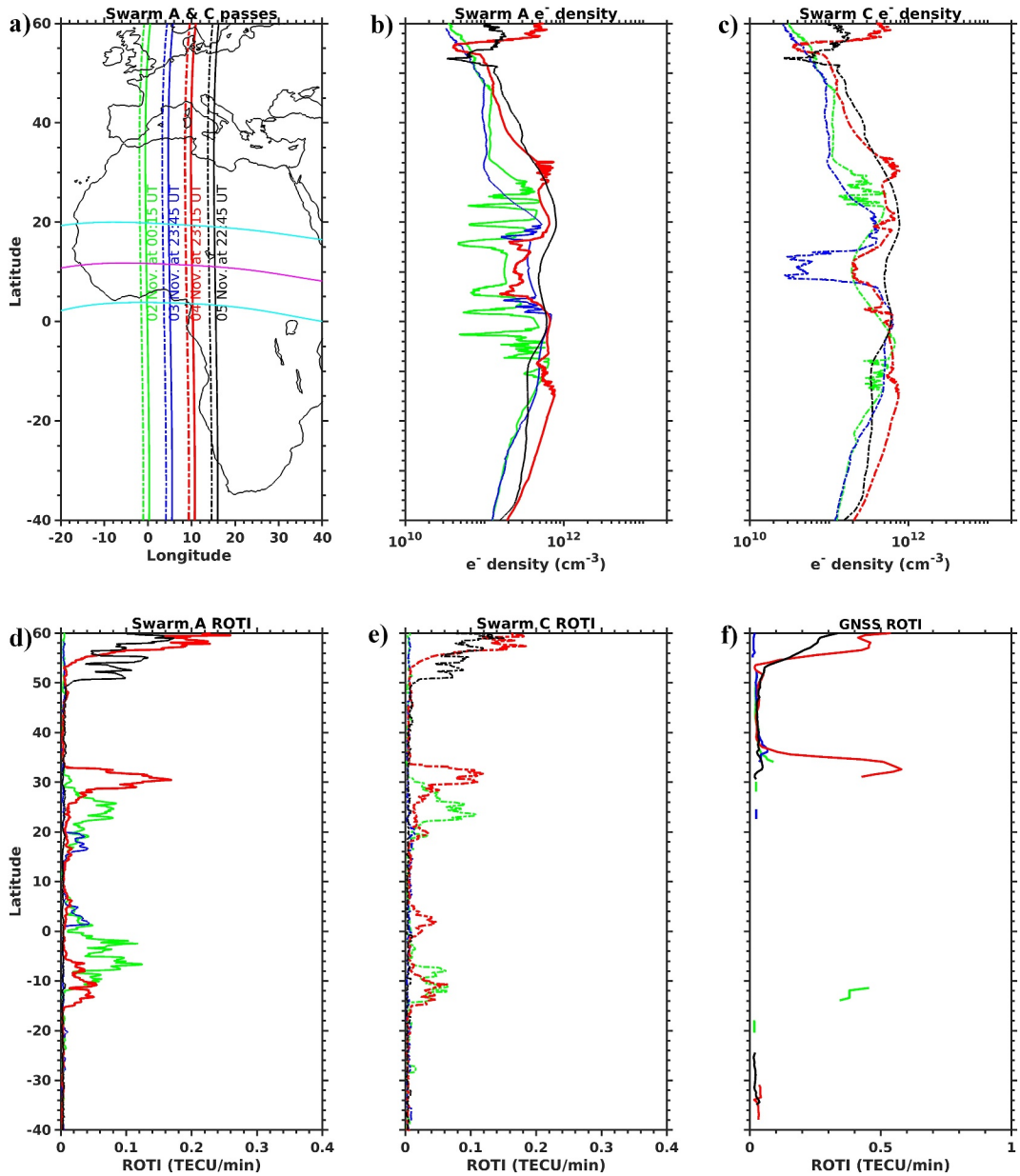

Figure 8. (a) Swarm A (thick lines) and C (dotted lines) passes across the African-European sector during 02–05 November 2023, and the approximate equator crossing time is also mentioned in the figure. (b), (c) electron density measured by Swarm A and (c) (d), (e) ROTI values derived from Swarm A and C topside total electron content data. (f) ROTI variation along Swarm satellite passes extracted from the ground-based GNSS-ROTI data.

or polarization electric fields could act as potential drivers of ROTI enhancement by generating MSTIDs during geomagnetically quiet periods.

In the present study, enhanced ROTI values of up to 0.8 TECU/min were observed in the mid-latitude region during a minor geomagnetic storm, without any evidence of MSTID activity (Figure 3) in the dTEC maps. At the same time, the ionosonde network using the High-Frequency Interferometry technique, Segarra et al. (2025) reported the occurrence of an LSTID starting at 19:20 UT, with an average period of 128 min, amplitude of 0.6 MHz, propagation velocity of 643 m/s, and direction of 226° (southwestward), lasting approximately 4 hr. However, only the northernmost stations—Juliusruh (JR055), Pruhonice (PQ052), Dourbes (DB049), and Sopron (SO148)—were strongly and continuously affected. Over the Roquetes ionosonde station, the LSTID signatures

disappeared by 22:00 UT. A detailed inspection of the dTEC maps revealed only a weak enhancement (below 0.2 TECU) in the high-mid latitudes of the European sector. In general, perturbations with amplitudes below 0.2 TECU are not considered TIDs (Tsugawa et al., 2018). Furthermore, it has been reported that LSTIDs typically cannot cause ROTI enhancement, as they do not involve small-scale plasma irregularities (Cherniak & Zakharenkova, 2018). Therefore, we conclude that the observed ROTI enhancements were not caused by the LSTIDs.

Further analysis using other ground-based observations and in situ Swarm measurements support that the enhanced ROTI was caused by a SPB generated in the low-latitude ionosphere. To date, such plasma bubbles have been reported only during moderate to strong geomagnetic storms (Aa et al., 2018; Campuzano et al., 2023; Cherniak & Zakharenkova, 2016). We observed the SPB during a minor geomagnetic activity in the post-equinoxial month, when the occurrence of plasma bubbles is typically lower than the equinox months, even in high solar activity years (Xiong et al., 2010).

The ROTI maps show a maximum geographical latitudinal extension up to 46°N around 5°W longitude. In the following section, we explore the plausible physical mechanisms behind the occurrence of the SPB on 04 November 2023.

4.1. Cause of the Super Plasma Bubble

It is well understood that the generalized RT instability mechanism could explain the generation of the EPB. However, prediction of the EPB occurrence is a challenging task because the generalized RT instability mechanism requires a seed perturbation. Many factors, such as external electric fields, the electric field coupling of the E-F region, the wave undulation at the bottom of the ionosphere, and transequatorial winds, could act as a potential seed for the generation of EPB (Bhattacharyya, 2022; Woodman, 2009).

Equatorial ionosphere often experiences pronounced post-sunset plasma irregularities during periods of geomagnetic disturbance attributed to the sudden entry of electric fields from higher latitudes, an occurrence commonly referred to as PPEF (Patra et al., 2016). Similarly, the generation of the plasma bubbles is also suppressed during the geomagnetic activity due to the disturbed dynamo electric fields (Sripathi et al., 2018). It has been reported that the penetration of electric fields over the equator can last for several hours without significant decay during the main phase of magnetic storms. Particularly, PPEFs can persist for longer periods when there is a strong southward IMF, enhanced solar wind, and a resulting strong duskward convection electric field (Huang et al., 2007; Kelley et al., 2003). The PPEF event can instigate positive and negative ionospheric storms in terms of enhanced or reduced TEC values in a region (Kapil & Seemala, 2024; Kuai et al., 2016). Positive storms usually occur when the eastward penetration electric field in the dusk sector augments the post-sunset eastward electric field, primarily due to the influence of the F-region dynamo. This effect, accentuated within the dusk longitude interval by height-integrated zonal conductivity gradients, results in a rapid uplift of the ionosphere during twilight hours. This uplift of the bottom of the ionosphere, in turn, triggers plasma instabilities leading to the plasma bubbles generation or bite-outs (Basu et al., 2007). Under suitable conditions, the high latitudinal extension of the plasma bubble requires larger vertical growth, which is controlled by the strength of the zonal E×B drift. Therefore, we have looked at the electric field variations obtained from the PPEFM model on 3–5 November 2023, which are shown in Figure 9. The PPEF, quiet time, and cumulative (PPEF + quiet) electric field variations during 03–05 November 2023 are shown in red, black, and green lines, respectively, in Figure 9. According to this model, the quiet time electric field is larger than the penetration electric fields on these days. From the model, it is evident that there are penetrated electric field peaks starting from 18:00 UT, which are in the temporal vicinity of the PRE observed. Additionally, the cumulative (quiet + penetration) electric field on November 4 is slightly higher than the day before and after.

The PPEF disturbances are conventionally measured by calculating the equatorial electrojet (EEJ). In the present case, due to the limited data coverage of magnetometer data in the African continent, we could not estimate the EEJ; however, its signature is mapped in the ΔH-component of Earth's magnetic field (Tsurutani et al., 2008). Nevertheless, to intensify the PPEF and background electric field effect, we look into the chain of magnetometer data from 50°N to 40°S, the chosen are shown in Figure 10. Figure 10 shows the ΔH values on the y-axis. The ΔH is calculated by removing the local half-hour mean of the solar quiet (Sq) variation from the H-component values, in order to eliminate the regular diurnal variation and highlight the storm-time disturbances more clearly. In Figure 10, green and red solid lines denote the quiet time mean (five quiet days averaged) and event time ΔH, and

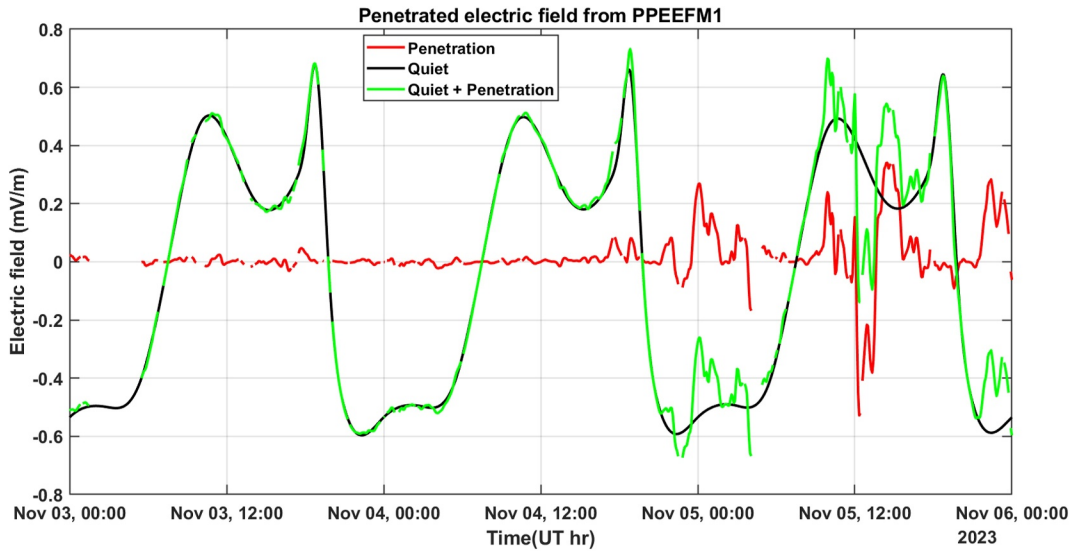

Figure 9. The prompt penetration electric field obtained from the prompt penetration equatorial electric field model model, across the 0°E longitude on 03, 04, and 05 November 2023. The red, green, and black lines show the penetrated, total, and quiet time electric field, respectively.

the gray solid region shows the upper and lower bounds of 2σ threshold calculated from quiet time mean values. The onset of disturbed time around 17:00 UT, negative ΔH is observed, with transient PPEF peaks. Prompt penetration electric field is a disruption of electric fields and currents, which are then transmitted from high to low latitudes simultaneously via geomagnetic field lines through the zeroth-order transverse magnetic (TM0) mode (Kikuchi et al., 2008). We observed along the European-African longitude, that is, 10°E ± 8° to analyze the PPEF variation. The magnetometer ΔH also shows a sharp reduction from 17:00 UT on 04 November 2023, covering mid to low latitudes, which also coincides with the onset of the minor geomagnetic storm (see Figure 10), and in general, during the main phase, the eastward electric field is enhanced (Huang et al., 2005). Earlier investigations showed that the E region electric field around 17:00 local time has a good positive correlation with the PRE (Ghosh et al., 2020).

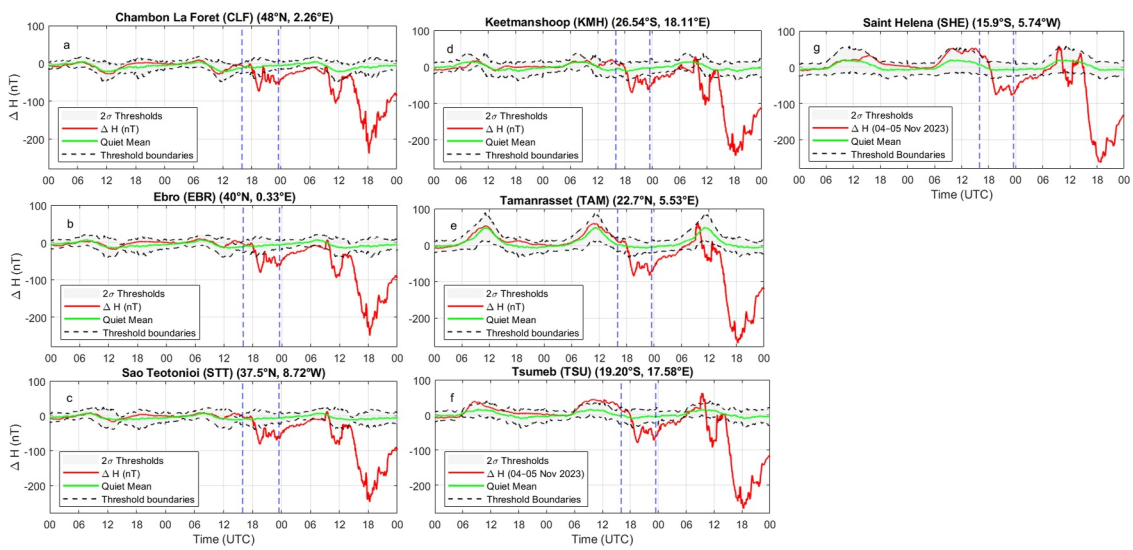

Figure 10. A series of ΔH values from the stations of low to mid latitudes is plotted, red solid lines show ΔH values of the day. The green solid line shows the mean of five international quiet days of ΔH values, whereas black dashed lines shaded with gray color show the 2σ upper and lower bound from the mean values of three consecutive days from 3 to 5 November 2023. The dashed blue shows the main phase period on 4 November 2023.

On 04th November, IMF Bz turned southward after 16:00 UT and it continues in the same state till 21:00 UT with small fluctuations, and the main phase of the geomagnetic storm was started at 18:00 UT (see Figure 2) and continued till midnight, and these changes is also concurrent with the PRE onset time. Simultaneous perturbations in the magnetic field were also observed in a chain of magnetometer observations from mid to low latitudes (in both hemisphere). Prompt penetration electric field model also shows a weak enhancement in the PPEF during this time. Furthermore, during the main phase, the PPEF associated eastward electric field is dominant (Huang et al., 2005), which can further support the PRE. All these observations evidence that PPEF impact also coincides with the PRE onset time, and the combination of both these effects could support the large vertical growth of the plasma bubble; as a result, the SPB could be generated. Interestingly, we also observed an intense EPB in the west African-European sector from the GOLD OI135.6 nm radiance images, and it is also longitudinally extended to Atlantic region. In a recent study, Aa et al. (2024) reported a SPB/bubble-like ionospheric super depletion structure during a strong geomagnetic storm. They also discussed various possibilities of the causes of these structures. One of them was PPEF-induced enhanced vertical drift.

Dabas et al. (2003) studied daytime EEJ strength and its correlation with some of the parameters like the virtual height of the F region (h'F), E ×B drift, the magnitude of post-sunset secondary maximum (PSSM) in electron content, which controls the day-to-day occurrence as well as the latitudinal/altitudinal growth of EPB. They suggested that the three most important parameters (h'F, E ×B, and PSSM) show a good correlation with daytime EEJ strength variations. The daytime ΔH component values observed on 04 November between 10:00 and 15:00 UT is higher than the average quiet time values as shown in Figure 10. A similar enhancement in ΔH component values was observed on 05 November (day 2) between early morning 12:00 UT and 08:00 UT. This increment persists with the variations depicted in Figure 10 for both days when compared to the quiet time variations as shown in Figure 10.

On the other hand, H component values show simultaneous variations during the main phase of the storm, that is, 17:00–23:30 UT on 04 November 2023. Additionally, the penetrated electric field is observed simultaneously in all the stations around 17:00 UT on 04 November 2023. This period of PPEF is close to PRE time, which can support the plasma instability caused by the post-sunset PRE, which may lead to generational and sustainable conditions for the SPB. On the other hand, on 05 November 2023, a sharp polarity change in the ΔH indicates the possibility of counter-electroject generation in the afternoon time, as shown in Figure 10, which may suppress the overall PRE effect (Uemoto et al., 2010). The enhanced ΔH component on 04 November supports that the large latitudinal extension of EIA on this night may primarily be driven by the E region dynamo, and followed by the weak geomagnetic storm associated with PPEF could support the higher vertical growth in the plasma bubble. As a consequence, these plasma bubbles reached up to 46°N. However, in order to reach 46°N, the plasma bubble at the low latitude should reach above 5,000 km apex altitude, which can not be explained by the linear growth rate of the RT instability, so we suggest that nonlinear processes were supporting the abrupt vertical growth of the low latitude plasma bubbles.

In general, an enhancement in the eastward electric field increases the vertical drift. As a consequence, the bottom of the ionospheric plasma is lifted to higher heights through E × B drift (Anderson et al., 2002). In the absence of direct drift measurements, the ionospheric variations can be inferred from the changes in the TEC values. Therefore, we examined the TEC variations on 04 November 2023 in comparison with the mean TEC of five geomagnetically quiet days. We also calculated their differences, as shown in Figure 11. The TEC data were obtained from the NASA CDAWeb database (https://cdaweb.gsfc.nasa.gov/). Figure 11 (left, middle, and right panels) illustrates the hourly mean TEC on 04 November 2023, the 5-day quiet-time mean TEC, and their corresponding differences, respectively, for every two-hour interval starting from 14:00 UT. From Figure 11, it can be observed that the TEC over the geomagnetic equator exhibits an enhancement of about 10–20 TECU until 18:00 UT. Afterward, the TEC in the equatorial region decreases, whereas the poleward edges of the EIA show an enhancement of approximately 10 TECU. The post-sunset EIA feature observed in Figure 11c indicates a significant modification in the equatorial electrodynamics during this period. shows there is latitudinal extension in the Northern crest of EIA above 20°N, as compared to the mean quiet time EIA shown in Figure 11b, suggesting increased post-sunset E × B drift. Furthermore, the PPEF caused by the minor storm could contribute to the generation, evolution, and sustainability of the SPB for a long time on this night.

Another interesting aspect of this study is that though the geomagnetic storm was strong on 05 November 2023, no EPB was observed on this day. Figure 9, we can notice a large variability in the PPEF, in particular around

10.1029/2025SW004659

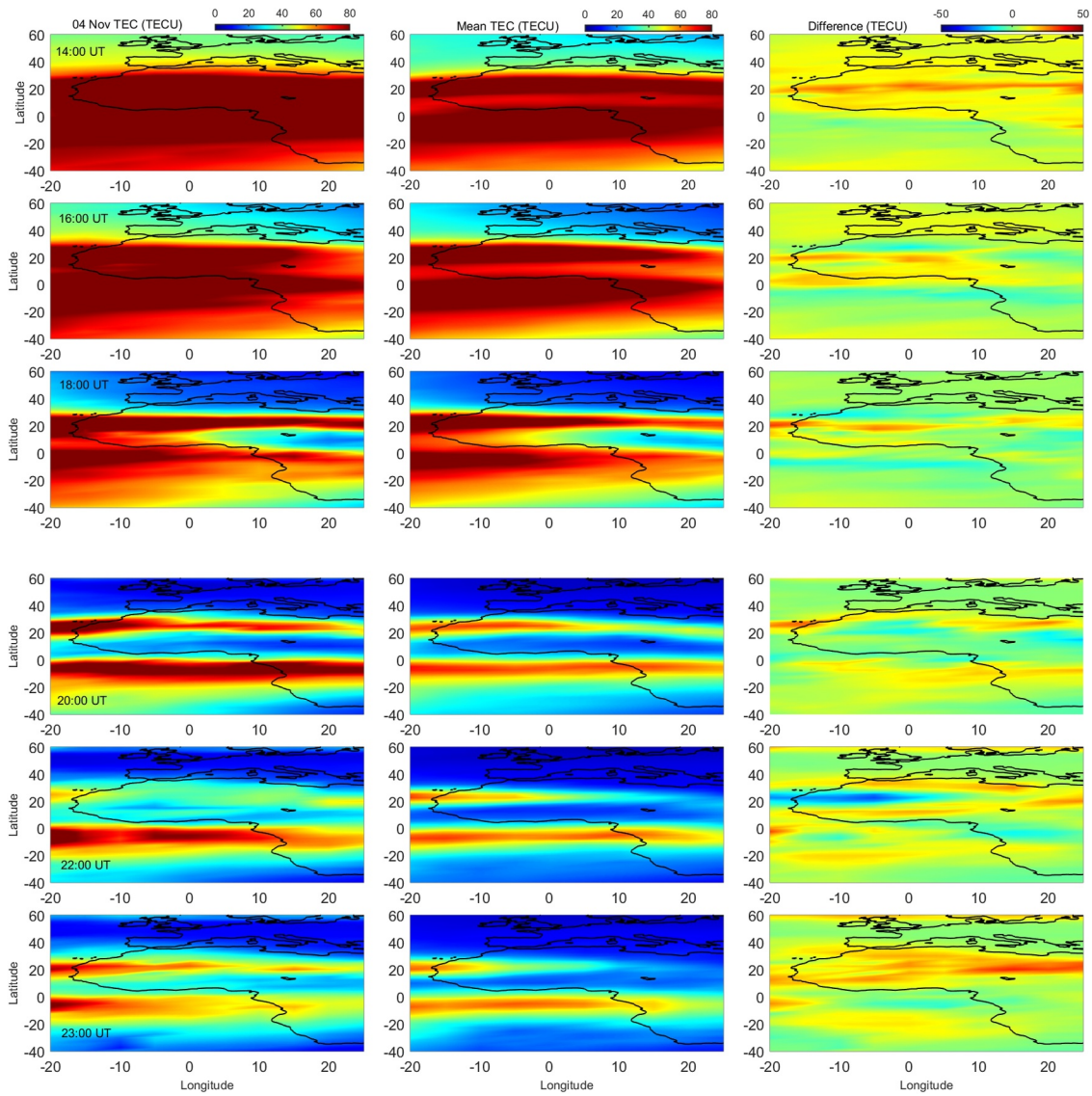

Figure 11. The Figure explains the equatorial ionization anomaly pattern over the European-African region. The *y*-axis shows the latitude illustrated with the background European-African coastlines; each row depicts the evolution over time from 14:00 UT to 23:00 UT, as presented in the figure. The figure shows three columns with total electron content (TEC) values on 04 November 2023, the mean TEC calculated from five international quiet days, and the last column shows their difference for 4 November 2023.

noon time, and polarity changes from negative to positive. Furthermore, the magnitude of the PPEF is almost zero during the sunset hours, which is the time when the PRE occurs. Similarly, the H component values were also negative during the interval of 15:00 to 20:00 UT on 05 November 2023 (shown in Figure 10), which means the CEJ was strong during this period, as shown in Figure 9. The westward electric field could effectively suppress the upward PRE (Uemoto et al., 2010). As a result, the plasma bubble could not be generated on 05 November 2023. The present study provides observational evidence of the SPB during a minor geomagnetic activity for the first time, which is investigated by the enhanced ROTI values in the mid-latitudinal region. An in-depth analysis using simultaneous GNSS-ROTI, ionosonde, Swarm A and C measurements, and GOLD OI135.6 nm emission irradiances, complemented with the low-latitude magnetometer data and PPEEFM model, reveals that the SPB is primarily driven by the combination of enhanced E-region dynamo electric field and minor storm-induced PPEF.

5. Summary

In this study, we investigate the cause of enhanced ROTI (0.8 TECU/min) values during a minor geomagnetic storm (Dst ≈ −50 nT, Kp = 4) in the western European region on 04 November 2023, which is rare. The investigation uses a suite of ground-based, space-based, and in situ observations, such as ionosonde, GNSS, Swarm, and GOLD satellites; a combination of these measurements covers the equator to mid-latitudes of both hemispheres.

1. The presence of strong range spread-Fs, TEC depletions, and in-situ moderate electron density depletions observed through Swarm satellite measurements indicates the occurrence of plasma bubbles without any evidence of MSTIDs. The appearance of plasma bubbles over an extended latitudinal range from 15°S to 40°N, together with moderate depletions in OI 135.6 nm emission irradiance, TEC, and in-situ electron density, along with strong range spread-F and enhanced ROTI values up to 46°N, clearly demonstrates the signature of the SPB presence.
2. The occurrence and possible generation mechanism of the SPB were investigated using multiple data sets, including magnetometer observations, empirical model simulations, and EIA analysis. This study presents evidence of a significant decrease in the evening time ΔH component on 04 November 2023 relative to the quiet-time mean values. Such a decrement during the minor geomagnetic storm indicates the arrival of the PPEF, which likely contributed to the extension of plasma bubbles into the mid-latitude region.
3. The findings suggest that the synergistic effects of enhanced PPEF, along with PRE, indicate a strengthened $E \times B$ drift that may have promoted the upward drift and broader spatial extent of plasma bubbles, thereby extending them beyond typical equatorial limits and resulting in the observed SPB. Additionally, the enhancement in nighttime EIA values is indicative of an increased $E \times B$ drift, which could result from an eastward PPEF. Since EEJ and in-situ drift measurements are unavailable for this event, we cannot conclusively quantify the PPEF effect; however, its occurrence is inferred from the PPEEFM model and magnetometer data. The observed nighttime EIA strengthening further supports the likelihood of a transient PPEF influence on SPB evolution.

This study provides new insights into the behavior of plasma bubbles during minor geomagnetic storms and their capacity to affect regions far beyond the equatorial zone, emphasizing the need to understand the underlying electrodynamic processes responsible for such events.

Conflict of Interest

The authors declare no conflicts of interest relevant to this study.

Data Availability Statement

The data needed to understand all the Figures in the text is as follows: Figure 2 is obtained using data from OMNI website https://omniweb.gsfc.nasa.gov/form/dx1.html. Global GNSS-TEC data processing has been supported by JSPS KAKENHI Grant 16H06286. Global navigation satellite system RINEX files for the GNSS-TEC processing are provided by many organizations listed on the webpage http://stdb2.isee.nagoya-u.ac.jp/GPS/GPS-TEC/gnss_provider_list.html. The ionograms are obtained from the Global Ionosphere Radio Observatory website. To access the ionogram data, select ionosonde URSI codes: EA036 (El Arenosillo), EB040 (Roquetes), and Ascension Island (AS00Q) from the following link https://giro.uml.edu/ionoweb/. The prompt penetration effect is evaluated from the model available at website https://geomag.colorado.edu/real-time-model-of-the-ionospheric-electric-fields. The INTERMAGNET magnetometer data is available at https://intermagnet.org/. The TEC data for the EIA results in Figure 11 can be obtained from the website https://cdaweb.gsfc.nasa.gov/.

Acknowledgments
One of the authors, Chandan Kapil (C.K.), would like to thank the SCOSTEP committee, Prof. Claudia Stolle (Director, IAP, Germany) for Granting the opportunity to visit IAP through the SCOSTEP visiting scholar (SVS) program at IAP, Kuhlunsborn, Germany. The author sincerely thanks Prof. A.P. Dimri, Director, IIG, India, for his constant support and Granting permission to visit IAP through SVS Program. We acknowledge Mr. Jens Mielich for his support in scaling the Ascension Island inogram. Global GNSS-TEC data processing has been supported by JSPS KAKENHI Grant 16H06286. Global navigation satellite system RINEX files for the GNSS-TEC processing are provided by many organizations listed on the webpage http://stdb2.isee.nagoya-u.ac.jp/GPS/GPS-TEC/gnss_provider_list.html. The results presented in this paper partially rely on data collected at magnetic observatories. We thank the national institutes that support them and INTERMAGNET for promoting high standards of magnetic observatory practice (www.intermagnet.org). Open Access funding enabled and organized by Projekt DEAL.

References

Aa, E., Huang, W., Liu, S., Ridley, A., Zou, S., Shi, L., et al. (2018). Midlatitude plasma bubbles over China and adjacent areas during a magnetic storm on 8 September 2017. *Space Weather*, *16*(3), 321–331. https://doi.org/10.1002/2017sw001776

Aa, E., Zhang, S.-R., Erickson, P. J., Vierinen, J., Coster, A. J., Goncharenko, L. P., et al. (2022). Significant ionospheric hole and equatorial plasma bubbles after the 2022 Tonga volcano eruption. *Space Weather*, *20*(7), e2022SW003101. https://doi.org/10.1029/2022SW003101

Aa, E., Zhang, S.-R., Zou, S., Wang, W., Wang, Z., Cai, X., et al. (2024). Significant midlatitude bubble-like ionospheric super-depletion structure (bliss) and dynamic variation of storm-enhanced density plume during the 23 April 2023 geomagnetic storm. *Space Weather*, *22*(3), e2023SW003704. https://doi.org/10.1029/2023SW003704

Akiyama, T., Yoshikawa, A., Fujimoto, A., & Uozumi, T. (2019). Relationship between plasma bubble and ionospheric current, equatorial electrojet, and equatorial counter electrojet. *Journal of physics: Conference series*, *1152*, 012022. https://doi.org/10.1088/1742-6596/1152/1/012022

Anderson, D. N., Anghel, A., Yumoto, K., Ishitsuka, M., & Kudeki, E. (2002). Estimating daytime vertical e × b drift velocities in the equatorial f-region using ground-based magnetometer observations. *Geophysical Research Letters*, *29*(12), 1596. https://doi.org/10.1029/2001GL014562

Astafyeva, E., Zakharenkova, I., & Alken, P. (2016). Prompt penetration electric fields and the extreme topside ionospheric response to the 22–23 June 2015 geomagnetic storm as seen by the swarm constellation. *Earth Planets and Space*, *68*, 1–12. https://doi.org/10.1186/s40623-016-0526-x

Bagiya, M. S., Sunil, A., Chakrabarty, D., & Sunda, S. (2017). Salient features of the dayside low latitude ionospheric response to the main phase step-i of the 17 March 2015 geomagnetic storm. *Advances in Space Research*, *60*(8), 1827–1837. https://doi.org/10.1016/j.asr.2017.06.010

Basu, S., Basu, S., Rich, F. J., Groves, K. M., MacKenzie, E., Coker, C., et al. (2007). Response of the equatorial ionosphere at dusk to penetration electric fields during intense magnetic storms. *Journal of Geophysical Research*, *112*(A8), A08308. https://doi.org/10.1029/2006JA012192

Bhattacharyya, A. (2022). Equatorial plasma bubbles: A review. *Atmosphere*, *13*(10), 1637. https://doi.org/10.3390/atmos13101637

Booker, H. G. (1938). Propagation of wave-packets incident obliquely upon a stratified doubly refracting ionosphere. *Philosophical Transactions of the Royal Society of London. Series A, Mathematical and Physical Sciences*, *237*(781), 411–451. https://doi.org/10.1098/rsta.1938.0012

Burke, W. J., Gentile, L. C., Huang, C. Y., Valladares, C. E., & Su, S. Y. (2004). Longitudinal variability of equatorial plasma bubbles observed by dmsp and rocsat-1. *Journal of Geophysical Research*, *109*(A12), A12301. https://doi.org/10.1029/2004JA010583

Cai, X., Burns, A. G., Wang, W., Coster, A., Qian, L., Liu, J., et al. (2020). Comparison of gold nighttime measurements with total electron content: Preliminary results. *Journal of Geophysical Research: Space Physics*, *125*(9), e2019JA027767. https://doi.org/10.1029/2019JA027767

Calabia, A., Imtiaz, N., Altadill, D., Yasyukevich, Y., Segarra, A., Prol, F. S., et al. (2024). Uncovering the drivers of responsive ionospheric dynamics to severe space weather conditions: A coordinated multi-instrumental approach. *Journal of Geophysical Research: Space Physics*, *129*(3), e2023JA031862. https://doi.org/10.1029/2023JA031862

Campuzano, S. A., Delgado-Gómez, F., Migoya-Orué, Y., Rodríguez-Caderot, G., Herraiz-Sarachaga, M., & Radicella, S. M. (2023). Study of ionosphere irregularities over the iberian peninsula during two moderate geomagnetic storms using gnss and ionosonde observations. *Atmosphere*, *14*(2), 233. https://doi.org/10.3390/atmos14020233

Cherniak, I., & Zakharenkova, I. (2016). First observations of super plasma bubbles in Europe. *Geophysical Research Letters*, *43*(21), 11137–11145. https://doi.org/10.1002/2016GL071421

Cherniak, I., & Zakharenkova, I. (2018). Large-scale traveling ionospheric disturbances origin and propagation: Case study of the December 2015 geomagnetic storm. *Space Weather*, *16*(9), 1377–1395. https://doi.org/10.1029/2018SW001869

Cherniak, I., & Zakharenkova, I. (2022). Development of the storm-induced ionospheric irregularities at equatorial and middle latitudes during the 25–26 August 2018 geomagnetic storm. *Space Weather*, *20*(2), e2021SW002891. https://doi.org/10.1029/2021SW002891

Collado-Villaverde, A., Muñoz, P., & Cid, C. (2024). Classifying and bounding geomagnetic storms based on the sym-h and asy-h indices. *Natural Hazards*, *120*(2), 1141–1162. https://doi.org/10.1007/s11069-023-06241-1

Dabas, R. S., Singh, L., Lakshmi, D. R., Subramanyam, P., Chopra, P., & Garg, S. C. (2003). Evolution and dynamics of equatorial plasma bubbles: Relationships to exb drift, postsunset total electron content enhancements, and equatorial electrojet strength. *Radio Science*, *38*(4), 141–1411. https://doi.org/10.1029/2001RS002586

DasGupta, A., Basu, S., Aarons, J., Klobuchar, J., Basu, S., & Bushby, A. (1983). Vhf amplitude scintillations and associated electron content depletions as observed at Arequipa, Peru. *Journal of Atmospheric and Terrestrial Physics*, *45*(1), 15–26. https://doi.org/10.1016/S0021-9169(83)80003-8

Dungey, J. (1956). The influence of the geomagnetic field on turbulence in the ionosphere. *Journal of Atmospheric and Terrestrial Physics*, *8*(1), 39–42. https://doi.org/10.1016/0021-9169(56)90089-7

Eastes, R. W., McClintock, W. E., Burns, A. G., Anderson, D. N., Andersson, L., Codrescu, M., et al. (2017). The global-scale observations of the limb and disk (gold) mission. *Space Science Reviews*, *212*(1), 383–408. https://doi.org/10.1007/s11214-017-0392-2

Ghosh, P., Otsuka, Y., Mani, S., & Shinagawa, H. (2020). Day-to-day variation of pre-reversal enhancement in the equatorial ionosphere based on gaia model simulations. *Earth Planets and Space*, *72*, 1–8. https://doi.org/10.1186/s40623-020-01228-9

Huang, C.-S., Foster, J. C., & Kelley, M. C. (2005). Long-duration penetration of the interplanetary electric field to the low-latitude ionosphere during the main phase of magnetic storms. *Journal of Geophysical Research*, *110*(A11). https://doi.org/10.1029/2005JA011202

Huang, C.-S., Sazykin, S., Chau, J. L., Maruyama, N., & Kelley, M. C. (2007). Penetration electric fields: Efficiency and characteristic time scale. *Journal of Atmospheric and Solar-Terrestrial Physics*, *69*(10–11), 1135–1146. https://doi.org/10.1016/j.jastp.2006.08.016

Kapil, C., & Seemala, G. K. (2024). Machine learning approach for detection of plasma depletions from Tec. *Advances in Space Research*, *73*(7), 3833–3844. https://doi.org/10.1016/j.asr.2023.04.042

Katamzi-Joseph, Z. T., Habarulema, J. B., & Hernández-Pajares, M. (2017). Midlatitude postsunset plasma bubbles observed over Europe during intense storms in April 2000 and 2001. *Space Weather*, *15*(9), 1177–1190. https://doi.org/10.1002/2017SW001674

Kelley, M. C., Ilma, R. R., Nicolls, M., Erickson, P., Goncharenko, L., Chau, J. L., et al. (2010). Spectacular low- and mid-latitude electrical fields and neutral winds during a superstorm. *Journal of Atmospheric and Solar-Terrestrial Physics*, *72*(4), 285–291. https://doi.org/10.1016/j.jastp.2008.12.006

Kelley, M. C., Makela, J. J., Chau, J. L., & Nicolls, M. J. (2003). Penetration of the solar wind electric field into the magnetosphere/ionosphere system. *Geophysical Research Letters*, *30*(4), 1158. https://doi.org/10.1029/2002GL016321

Kikuchi, T., Hashimoto, K. K., & Nozaki, K. (2008). Penetration of magnetospheric electric fields to the equator during a geomagnetic storm. *Journal of Geophysical Research*, *113*(A6), A06214. https://doi.org/10.1029/2007JA012628

Kim, J.-H., & Chang, H.-Y. (2018). Geomagnetic field variations observed by intermagnet during 4 total solar eclipses. *Journal of Atmospheric and Solar-Terrestrial Physics*, *172*, 107–116. https://doi.org/10.1016/j.jastp.2018.03.023

King, G. (1970). Spread-f on ionograms. *Journal of Atmospheric and Terrestrial Physics*, *32*(2), 209–221. https://doi.org/10.1016/0021-9169(70)90192-3

Kotulak, K., Zakharenkova, I., Krankowski, A., Cherniak, I., Wang, N., & Fron, A. (2020). Climatology characteristics of ionospheric irregularities described with gnss roti. *Remote Sensing*, *12*(16), 2634. https://doi.org/10.3390/rs12162634

Kuai, J., Liu, L., Liu, J., Sripathi, S., Zhao, B., Chen, Y., et al. (2016). Effects of disturbed electric fields in the low-latitude and equatorial ionosphere during the 2015 st. Patrick's day storm. *Journal of Geophysical Research: Space Physics*, *121*(9), 9111–9126. https://doi.org/10.1002/2016JA022832

Li, G., Ning, B., Wang, C., Abdu, M., Otsuka, Y., Yamamoto, M., et al. (2018). Storm-enhanced development of postsunset equatorial plasma bubbles around the Meridian 120°e/60°w on 7–8 September 2017. *Journal of Geophysical Research: Space Physics*, *123*(9), 7985–7998. https://doi.org/10.1029/2018JA025871

Ma, G., & Maruyama, T. (2006). A super bubble detected by dense gps network at East Asian longitudes. *Geophysical Research Letters*, *33*(21). https://doi.org/10.1029/2006gl027512

Manoj, C., & Maus, S. (2012). A real-time forecast service for the ionospheric equatorial zonal electric field. *Space Weather*, *10*(S09002). https://doi.org/10.1029/2012SW000825

Martinis, C., Baumgardner, J., Mendillo, M., Wroten, J., Coster, A., & Paxton, L. (2015). The night when the auroral and equatorial ionospheres converged. *Journal of Geophysical Research: Space Physics*, *120*(9), 8085–8095. https://doi.org/10.1002/2015JA021555

Narayanan, V. L., Taori, A., Patra, A. K., Emperumal, K., & Gurubaran, S. (2012). On the importance of wave-like structures in the occurrence of equatorial plasma bubbles: A case study. *Journal of Geophysical Research*, *117*(A1). https://doi.org/10.1029/2011JA017054

Otsuka, Y., Ogawa, T., Saito, A., Tsugawa, T., Fukao, S., & Miyazaki, S. (2002). A new technique for mapping of total electron content using gps network in Japan. *Earth Planets and Space*, *54*(1), 63–70. https://doi.org/10.1186/BF03352422

Patra, A. K., Chaitanya, P. P., Dashora, N., Sivakandan, M., & Taori, A. (2016). Highly localized unique electrodynamics and plasma irregularities linked with the 17 March 2015 severe magnetic storm observed using multitechnique common-volume observations from gadanki, India. *Journal of Geophysical Research: Space Physics*, *121*(11), 11518–11527. https://doi.org/10.1002/2016JA023384

Patra, A. K., Taori, A., Chaitanya, P. P., & Sripathi, S. (2013). Direct detection of wavelike spatial structure at the bottom of the f region and its role on the formation of equatorial plasma bubble. *Journal of Geophysical Research: Space Physics*, *118*(3), 1196–1202. https://doi.org/10.1002/jgra.50148

Paul, K. S., Haralambous, H., Oikonomou, C., Paul, A., Belehaki, A., Ioanna, T., et al. (2018). Multi-station investigation of spread f over Europe during low to high solar activity. *Journal of Space Weather and Space Climate*, *8*, A27. https://doi.org/10.1051/swsc/2018006

Paul, K. S., Haralambous, H., Oikonomou, C., Singh, A., Gulyaeva, T., Panchenko, V., et al. (2023). Mid-latitude spread f over an extended European area. *Journal of Atmospheric and Solar-Terrestrial Physics*, *248*, 106093. https://doi.org/10.1016/j.jastp.2023.106093

Paul, K. S., Haralambous, H., Singh, A. K., Gulyaeva, T. L., & Panchenko, V. A. (2022). Mid-latitude spread f long-term occurrence characteristics as a function of latitude over Europe. *Journal of Atmospheric and Solar-Terrestrial Physics*, *70*(3), 710–722. https://doi.org/10.1016/j.asr.2022.05.022

Paul, K. S., Rafi, M. H., Haralambous, H., & Mostafa, M. G. (2024). Correlation of rate of Tec index and spread f over European ionosondes. *Atmosphere*, *15*(3), 331. https://doi.org/10.3390/atmos15030331

Pi, X., Mannucci, A. J., Lindqwister, U. J., & Ho, C. M. (1997). Monitoring of global ionospheric irregularities using the worldwide gps network. *Geophysical Research Letters*, *24*(18), 2283–2286. https://doi.org/10.1029/97gl02273

Rajesh, P. K., Lin, C. C. H., Lin, J. T., Lin, C. Y., Liu, J. Y., Matsuo, T., et al. (2022). Extreme poleward expanding super plasma bubbles over Asia-Pacific region triggered by Tonga volcano eruption during the recovery-phase of geomagnetic storm. *Geophysical Research Letters*, *49*(15), e2022GL099798. https://doi.org/10.1029/2022GL099798

Seemala, G. K., & Valladares, C. E. (2011). Statistics of total electron content depletions observed over the South American continent for the year 2008. *Radio Science*, *46*(5), 1–14. https://doi.org/10.1029/2011RS004722

Segarra, A., Altadill, D., de Paula, V., & Navas-Portella, V. (2025). Climatology of large-scale traveling ionospheric disturbances above Europe during the 2014–2023 period. *Journal of Space Weather and Space Climate*, *15*, 28. https://doi.org/10.1051/swsc/2025024

Shiokawa, K., Ihara, C., Otsuka, Y., & Ogawa, T. (2003). Statistical study of nighttime medium-scale traveling ionospheric disturbances using midlatitude airglow images. *Journal of Geophysical Research*, *108*, A1. https://doi.org/10.1029/2002ja009491

Singh, S., Johnson, F. S., & Power, R. A. (1997). Gravity wave seeding of equatorial plasma bubbles. *Journal of Geophysical Research*, *102*(A4), 7399–7410. https://doi.org/10.1029/96JA03998

Sivakandan, M., Mondal, S., Sarkhel, S., Chakrabarty, D., Sunil Krishna, M. V., Chaitanya, P. P., et al. (2020). Mid-latitude spread-f structures over the geomagnetic low-mid latitude transition region: An observational evidence. *Journal of Geophysical Research: Space Physics*, *125*(5), e2019JA027531. https://doi.org/10.1029/2019JA027531

Sivakandan, M., Paulino, I., Ramkumar, T., Taori, A., Patra, A., Sripathi, S., et al. (2019). Multi-instrument investigation of troposphere-ionosphere coupling and the role of gravity waves in the formation of equatorial plasma bubble. *Journal of Atmospheric and Solar-Terrestrial Physics*, *189*, 65–79. https://doi.org/10.1016/j.jastp.2019.04.006

Sori, T., Otsuka, Y., Shinbori, A., Nishioka, M., & Perwitasari, S. (2022). Geomagnetic conjugacy of plasma bubbles extending to mid-latitudes during a geomagnetic storm on March 1, 2013. *Earth Planets and Space*, *74*(1), 120. https://doi.org/10.1186/s40623-022-01682-7

Sripathi, S., Banola, S., Emperumal, K., Suneel Kumar, B., & Radicella, S. M. (2018). The role of storm time electrodynamics in suppressing the equatorial plasma bubble development in the recovery phase of a geomagnetic storm. *Journal of Geophysical Research: Space Physics*, *123*(3), 2336–2350. https://doi.org/10.1002/2017JA024956

Sultan, P. J. (1996). Linear theory and modeling of the rayleigh-taylor instability leading to the occurrence of equatorial spread f. *Journal of Geophysical Research*, *101*(A12), 26875–26891. https://doi.org/10.1029/96JA00682

Tsugawa, T., Nishioka, M., Ishii, M., Hozumi, K., Saito, S., Shinbori, A., et al. (2018). Total electron content observations by dense regional and worldwide international networks of Gnss. *Journal of Disaster Research*, *13*(3), 535–545. https://doi.org/10.20965/jdr.2018.p0535

Tsunoda, R. T. (2010). On seeding equatorial spread F: Circular gravity waves. *Geophysical Research Letters*, *37*(10). https://doi.org/10.1029/2010GL043422

Tsurutani, B. T., Verkhoglyadova, O. P., Mannucci, A. J., Saito, A., Araki, T., Yumoto, K., et al. (2008). Prompt penetration electric fields (PPEFs) and their ionospheric effects during the great magnetic storm of 30–31 October 2003. *Journal of Geophysical Research*, *113*, A05311. https://doi.org/10.1029/2007ja012879

Uemoto, J., Maruyama, T., Saito, S., Ishii, M., & Yoshimura, R. (2010). Relationships between pre-sunset electrojet strength, pre-reversal enhancement and equatorial spread-f onset. In *Annales Geophysicae* (Vol. 28(2), pp. 449–454). Copernicus Publications. https://doi.org/10.5194/angeo-28-449-2010

Woodman. (2009). Spread F–An old equatorial aeronomy problem finally resolved? In *Annales Geophysicae* (Vol. 27(5), pp. 1915–1934). https://doi.org/10.5194/angeo-27-1915-2009

Xiong, C., Park, J., Luhr, H., Stolle, C., & Ma, S. Y. (2010). Comparing plasma bubble occurrence rates at champ and grace altitudes during high and low solar activity. In *Annales Geophysicae* (Vol. 28(9), pp. 1647–1658). Copernicus Publications. https://doi.org/10.5194/angeo-28-1647-2010